Inorganic Chemistry
Article
pubs.acs.org/IC

Molecular Co(II) and Co(III) Heteroarylalkenolates as Efficient Precursors for Chemical Vapor Deposition of Co_3O_4 Nanowires

Mehtap Büyükyazi,[†] Corinna Hegemann,[†] Thomas Lehnen,[†] Wieland Tyrra,[†] and Sanjay Mathur*,[†,‡]

[†]Institute of Inorganic Chemistry, University of Cologne, Greinstrasse 6, Cologne 50939, Germany
[‡]International Research Center for Renewable Energy, School of Energy & Power Engineering, Xian Jiaotong University, Xian, Shaanxi 710049, P. R. China

Supporting Information

ABSTRACT: Two new cobalt precursors, $Co^{II}(PyCHCOCF_3)_2(DMAP)_2$ (**1**) and $Co^{III}(PyCHCOCF_3)_3$ (**2**), based on Co(II) and Co(III) centers were synthesized using a redox active ligand system. The different chemical configurations of **1** and **2** and differential valence states of cobalt were confirmed by crystal structure determination and comprehensive analytical studies. Whereas **1** could not be studied by NMR due to the paramagnetic nature of the central atom, **2** was unambiguously characterized by multinuclear 1D and 2D NMR experiments in solution. Both compounds are efficient precursors for catalyst-free growth of Co_3O_4 nanowires on Si and Al_2O_3 substrates by a chemical vapor deposition process. The different valence states of cobalt species influenced their chemical decomposition pathways in the gas phase; for instance, **1** was partially oxidized ($Co^{2+} \rightarrow Co^{3+}$), and **2** underwent reduction ($Co^{3+} \rightarrow Co^{2+}$) to form pure cobaltite in both cases that verified the metal−ligand redox interplay. Co_3O_4 nanowires with nanometric diameters (50−100 nm) were obtained irrespective of the chosen cobalt precursor. Investigations on the humidity sensing behavior of CVD deposits demonstrated their potential as promising sensor materials.

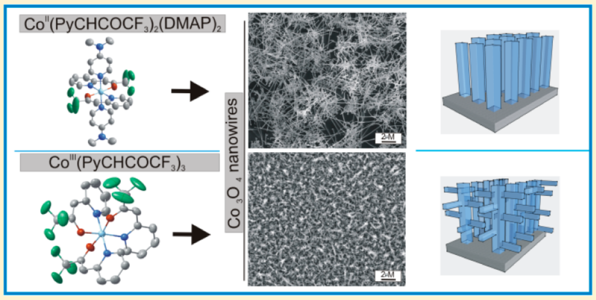

INTRODUCTION

The cobalt−oxygen binary phase diagram shows a rich and diverse structural chemistry with CoO, Co_3O_4, and Co_2O_3 as the major phases. Whereas Co_3O_4 and CoO represent the stable oxides of cobalt, Co_2O_3 appears to be stable only at low temperatures or under high oxygen partial pressure.[1,2] CoO with the rock salt structure is more stable at higher temperatures than Co_3O_4, which starts to decompose at about 1170 K into CoO. In recent years, cobalt oxides especially Co_3O_4 have been studied extensively as promising candidates for their use as catalysts,[3,4] electrochemical capacitors,[5,6] anode materials in lithium-ion battery,[7,8] and gas sensors,[9,10] as well as in water splitting applications due to the inherent ability of cobalt to produce reactive oxygen species.[11] In particular, nanostructured Co_3O_4 materials are of special interest in their good sensing performances in detecting various and volatile organic chemicals (VOCs) such as ethanol, xylene, and acetone with rapid and high response signals at low operating temperatures.[12,13] In view of their application potential, Co_3O_4 nanoparticles, nanofilms, and nanowires were recently synthesized by several approaches including solvothermal syntheses,[14,15] electrospinning,[16,17] and chemical vapor deposition (CVD).[18−23] In comparison to established methods enabling growth of large number of transition metal oxides by vapor phase techniques,[24−27] reports on cobalt oxides are limited mainly due to the lack of stable cobalt precursors with adequate stability and volatility.[28] The known cobalt complexes such as $HCo(CO)_4$, $Co_2(CO)_8$, $CoCF_3(CO)_4$, $CpCo(CO)_2$, and $CoNO(CO)_3$ show low thermal stability and undesired reactions in the gas phase resulting in nonreproducible Co:O stoichiometries in CVD deposits.[29−31] In addition, no cobalt oxide formation could be observed by using these cobalt precursors in CVD processes, and frequently, Co or $CoSi_2$ films were deposited at temperatures below 750 °C on different substrates.[29−31] In addition, the lack of Co−O bonds in the precursor molecules often produces oxygen deficient phases and further promotes incorporation of heteroatoms (N, C) present in the ligand periphery. We have recently reported on the use of a new ligand system based on a substituted heteroarylalkenoles, which through electronic push−pull effects, induced by electron-withdrawing perfluoroalkyl groups ($-CF_3$, $-C_2F_5$, $-C_3F_7$) and electron-donating aromatic units ($-C_5NH_4$ (Py), $-Me_2C_3NO$, $-Me_2C_3NS$), offer a new class of metallic and oxide precursors (Figure 1).[32−35]

In this work, a pyridine-substituted alkenol ($PyCHCOHCF_3$) was used as a bidentate ligand to obtain stable Co(II) and Co(III) molecular precursors, which were synthesized by modifying a published procedure and structurally characterized for the first time.[36] We report herein the deposition of phase-pure Co_3O_4 using cobalt alkenolates, when compared to other cobalt complexes such as $Co(dpm)_2$

Received: May 21, 2014
Published: October 2, 2014

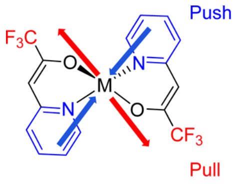

Figure 1. Electronic effects active in the stabilization of cobalt(II) heteroarylalkenolate.

(Hdpm = 2,2,6,6-tetramethyl-3,5-heptanedione) and $Co(hfa)_2\cdot 2H_2O$ (hfa = 1,1,1,5,5,5-hexafluoro-2,4-pentanedione) that often produced a mixture of different cobalt oxides.[37,38] Typically, CoO, Co_3O_4, or a mixture of both metal oxides were persistent at low temperatures (350−500 °C). In addition, we demonstrate the first catalyst-free growth of the Co_3O_4 nanowires as a pure phase at 800 °C from the new cobalt precursors $Co^{II}(PyCHCOCF_3)_2(DMAP)_2$ (**1**) and $Co^{III}(PyCHCOCF_3)_3$ (**2**), in which the Co−O units are pre-existent. Because of their high volatility and thermal stability, these cobalt complexes were found to be suitable for chemical vapor growth of Co_3O_4 nanostructures exhibiting excellent humidity sensing properties.

■ EXPERIMENTAL SECTION

Chemicals and Methods. DMAP (4-dimethylaminopyridin 99%), NaOH, and $Co^{II}(OOCCH_3)_2\cdot 4H_2O$ were purchased from Acros Organics and used without further purification. Data collection for X-ray structure elucidation was performed on a STOE IPDS I and II diffractometer using graphite-monochromated Mo Kα radiation (0.710 73). The programs used in this work are STOE's *X-Area*,[39] and the *WINGX* suite of programs,[40] including *SIR-92*[41] and *SHELXL-97*,[42] for structure solution and refinement. Microanalysis for C, H, and N contents was carried out using a HEKAtech CHNS EuroEA 3000 analyzer. NMR spectra were recorded at 298 K on a Bruker AVANCE II 300 spectrometer equipped with a BBFO Z-gradient probe head with NMR spectroscopic frequencies as follows: ^1H, 300.13 MHz (TMS); ^{13}C, 75.46 MHz (TMS); ^{19}F, 282.37 MHz (CCl_3F). Assignment of all ^1H (400.13 MHz, TMS), ^{13}C (100.61 MHz, TMS), ^{19}F (376.50 MHz, CCl_3F), and ^{15}N (43.36 MHz) NMR signals to each ligand molecule in compound $Co^{III}(PyCHCOCF_3)_3$ (**2**) was elucidated by 2D experiments on Bruker Avance II 300, Bruker Avance 400, and Bruker Avance II$^+$ 600 spectrometers at 298 K. ^{59}Co spectrum ($K_3Co(CN)_6$) was recorded on a Bruker Avance II$^+$ spectrometer equipped with a TBI probe with Z-gradient. Temperature was set to 298 K. Fourier transform infrared (FT-IR) measurements were recorded on a PerkinElmer Spectrum 400. EI-MS spectra were obtained on a Finnigan MAT 95 (20 eV) in *m*/*z* (relative percentage), operating in positive ion modes. Thermal analyses were performed on a TGA/DSC 1 (Mettler-Toledo-GmbH, Germany) in an air atmosphere (25 mL/min) at a rate of 10 °C/min from 30 to 620 °C. The weight of the sample was in the range 4−5 mg. UV−vis spectra were carried out with a Lambda 950 (PerkinElmer) device between 250 and 800 nm on 1,2-dichloroethane solutions using quartz cuvettes. Room temperature powder X-ray diffraction (XRD) was obtained on a STOE-STADI MP diffractometer operating in a reflection mode using Cu Kα (λ = 1.5418 Å) radiation.

Synthesis of $Co^{II}(PyCHCOCF_3)_2(DMAP)_2$ (1). The organic ligand $PyCHCOHCF_3$ was prepared according to reported procedure.[35] $Co^{II}(PyCHCOCF_3)_2(DMAP)_2$ (**1**) was synthesized by dissolving 0.5 g (2 mmol) of $Co^{II}(OOCCH_3)_2\cdot 4H_2O$ and 0.49 g (4 mmol) of DMAP in water. Subsequently, 0.76 g (4 mmol) of $PyCHCOHCF_3$ and 0.16 g (2 mmol) of NaOH in a mixture of ethanol and water was added dropwise to the solution of $Co^{II}(OOCCH_3)_2\cdot 4H_2O$ in water. After 2 h of stirring at room temperature, the reaction mixture was filtered to obtain a yellow compound. The sublimation (130 °C, 10^{-3} mbar) led to $Co^{II}(PyCHCOCF_3)_2(DMAP)_2$ as purified yellow product. Yield: 1.0 g (75%). CHNS Anal. Calcd: C, 53.0; N, 12.3; H, 4.4. Found: C, 54.1; N, 12.3; H, 4.6. EI-MS: 435 (100, M$^+$ − 2DMAP), 366 (12, M$^+$ − CF_3 − 2DMAP), 247 (8, M$^+$ − $PyCHCOCF_3$ − 2DMAP), 122 (70, DMAP) %. IR (cm^{-1}): ν(C═O) 1617, ν(C═C) 1548, 1535, ν(CF) 1100, γ(═CH) 807. UV−vis (1,2-dichloroethane, λ_{max}/nm): 264, 280, 361, 612−696.

Synthesis of $Co^{III}(PyCHCOCF_3)_3$ (2). The cobalt(III) complex **2** was obtained by the reaction of 5.34 g (6 mmol) of $PyCHCOHCF_3$ (L) with 0.5 g (2 mmol) of $Co^{II}(OOCCH_3)_2\cdot 4H_2O$ in ethanol (Supporting Information Figure S 1). The reaction mixture was stirred for 12 h at room temperature. Solvent removal at reduced pressure yielded a pale brown solid. The raw material was purified by sublimation (140 °C, 10^{-3} mbar) to obtain **2** as dark green powder.

Yield: 0.9 g (72%). CHNS Calcd: C, 46.0; N, 6.7; H, 2.4. Found: C, 45.7; N, 6.1; H, 2.5. ^{59}Co NMR (142.39 MHz, acetone-d_6, 298 K, δ/ppm): +11 095 ($\Delta_{1/2} \approx$ 360 MHz). ^1H NMR (300.13 MHz, acetone-d_6, 298 K, δ/ppm): 8.11 (d, 1H, 1-H, L 1), 7.87−7.86 (overlapping m, 2H, 1-H and 3-H, L 3 and L 1), 7.82 (t, 1H, 3-H, L 3), 7.73 (t, 1H, 3-H, L 2), 7.46−7.42 (overlapping m, 2H, 1-H and 4-H, L 2 and L 3), 7.29 (d, 1H, 4-H, L 1), 7.23 (t, 1H, 2-H, L 1), 7.18 (d, 1H, 4-H, L 2), 7.08 (t, 2-H, L 2), 6.99 (t, 1H, 2-H, L 1), 6.27 (s, 1H, 6-H, L 3), 6.07 (s, 1H, 6-H, L 2), 5.89 (s, 1H, 6-H, L 1). $^{13}C\{H\}$ NMR (75.46 MHz, acetone-d_6, 298 K, δ/ppm): 156.7 (5-C, L 1), 156.6 (5-C, L 2), 155.8 (5-C, L 3), 155.7 (7-C, L 2), 155.2 (7-C, L 1), 153.6 (7-C, L 3), 151.8 (1-C, L 2), 151.5 (1-C, L 1), 150.4 (1-C, L 3), 140.1 (3-C, L 1), 139.4 (3-C, L 3), 138.9 (3-C, L 2), 124.1 (4-C, L 3), 123.8 (4-C, L 1), 122.6 (2-C, L 1), 122.4 (4-C, L 2), 121.3 (2-C, L 3), 121.0 (2-C, L 2), 117.5 (8-C, L 2), 117.5 (8-C, L 3), 117.1 (8-C, L 1), 97.1 (6-C, L 2), 97.1 (6-C, L 3), 95.9 (6-C, L 1). ^{19}F NMR (282.4 MHz, acetone-d_6, 298 K, δ/ppm): −73.10 (s, L 3), −72.83 (s, L 2), −72.80 (s, L 1). ^{15}N NMR (43.37 MHz, acetone-d_6, 298 K, δ/ppm): 195 (s, L 3), 188 (s, L 2), 180 (s, L 1). EI-MS: 623 (15, M$^+$), 435 (100, M$^+$ − $PyCHCOCF_3$), 366 (10, M$^+$ − $PyCHCOCF_3$ − CF_3), 189 (40, $PyCHCOCF_3$), 120 (32, $PyCHCO^+$), 92 (15, $PyCH_2^+$) %. IR (cm^{-1}): ν(C═O) 1619, ν(C═C) 1556, 1541, ν(CF) 1107, γ(═CH) 808. UV−vis (1,2-dichloroethane, λ_{max}/nm): 261, 292, 365, 606.

CVD of Co_3O_4. Cobalt oxide nanowires were deposited on Si and Al_2O_3 substrates using horizontal CVD reactor in which a high frequency field was used to inductively heat the substrates by placing them on a graphite susceptor maintained at 800 °C. During the deposition process oxygen was introduced in the system to facilitate the formation of cobalt oxide. The precursors were introduced in the reactor through a glass flange by applying vacuum (10^{-3} mbar) for 90 min and heating the precursors $Co^{II}(PyCHCOCF_3)_2(DMAP)_2$ and $Co^{III}(PyCHCOCF_3)_3$ to 140 and 150 °C, respectively (Figure 2).

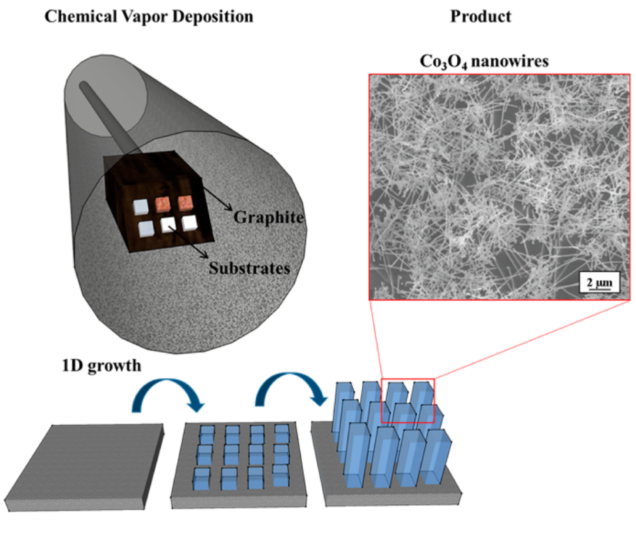

Figure 2. Schematic representation of the chemical vapor deposition of Co_3O_4 nanowires with synthesized Co(II) and Co(III) heteroarylalkenolates.

Scheme 1. Synthetic Route to Cobalt Heteroarylalkenolates $Co^{II}(PyCHCOCF_3)_2(DMAP)_2$ (1) and $Co^{III}(PyCHCOHCF_3)_3$ (2)

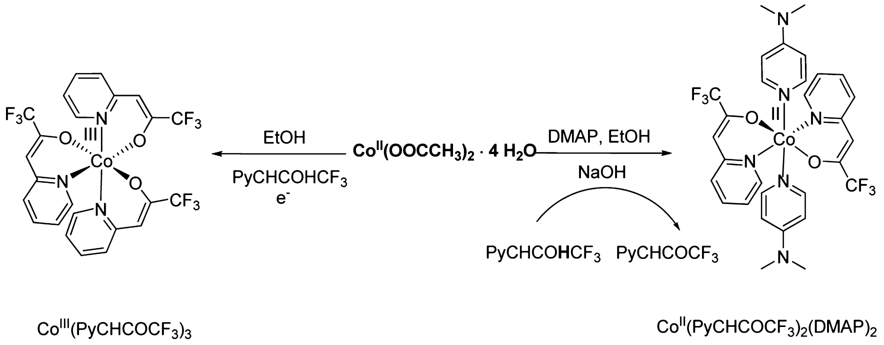

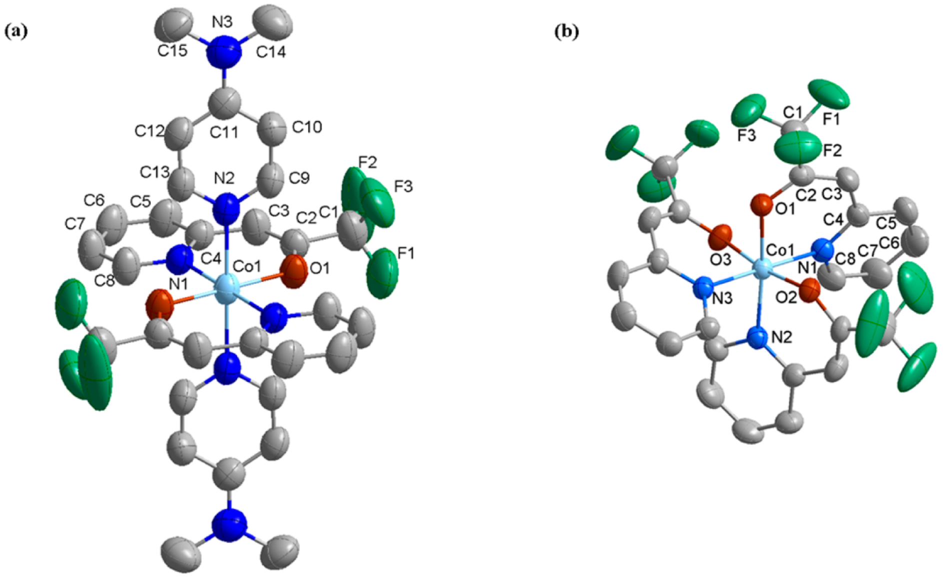

Figure 3. Molecular structure of (a) $Co^{II}(PyCHCOCF_3)_2(DMAP)_2$ (**1**) and (b) $Co^{III}(PyCHCOCF_3)_3$ (**2**) (hydrogen atoms are omitted for clarity). Thermal ellipsoids are shown at 50% probability level.

Materials Characterization. X-ray photoemission spectroscopy (XPS) was performed on ESCA M-Probe (Al Kα) with an energy resolution of 0.8 eV. Raman spectroscopy was performed with a Renishaw 514 nm argon laser. Scanning electron microscopy (SEM) was executed on a FEI Nova NanoSEM 430 scanning electron microscope. Transmission electron microscopy (HR-TEM) was performed with HR-TEM Philips CM 300/UT-System (300 kV). The sensing properties were determined with the aid of a self-designed measurement system operated at 30 °C using Area FC-7700C mass flow controller and Keithley 2400 source meter, both controlled by LabView software. Formation of ohmic contacts was achieved by dc sputtering of interdigitated gold electrodes (30 mA, 4 min) on opposing edges of the Co_3O_4 nanostructure arrays on alumina substrates. TEM samples were prepared by scratching off the deposited nanowires with a sharp blade followed by sonification of Co_3O_4 nanowires in ethanol for 30 s. The obtained suspension was drop-casted on carbon-coated copper TEM grids (Quantifoil Micro Tools GmbH, Jena, Germany). Formation of ohmic contacts was achieved sputtering gold electrodes (Emitech K550; 30 mA, 4 min) on opposing edges of the Co_3O_4 nanostructure arrays deposited on alumina substrates. The sensing properties were determined with the aid of a self-designed measurement system operating at 30 °C using a source meter (Keithley 2400) to monitor correlations between resistivity and relative humidity.[43,44] Different humidity concentrations in the gas stream have been achieved via variation of the ratio between saturated steam (distilled water) and synthetic air (Linde) while keeping the gas flow rate constant at 200 sccm. The heating unit, source meter, and both mass flow controllers (Area FC-7700C) were controlled by the LabView software.

■ RESULTS AND DISCUSSION

Synthesis and Characterization of Precursors. The synthetic procedure of the Co(II) and Co(III) heteroarylalkenolates is outlined in Scheme 1. The Co(II) species, $Co^{II}(PyCHCOCF_3)_2(DMAP)_2$ (**1**), was obtained by the reaction of cobalt(II) acetate tetrahydrate with 2 equiv of deprotonated ligand 3,3,3-trifluoro-1-(pyridine-2-yl)propen-2-ol, ($PyCHCOHCF_3$), in a mixture of ethanol, water, and DMAP. The chelating ligand with O- and N-donor sites binds to the cobalt center in a bidentate fashion resulting in a stable six-membered metallacycle. The observed octahedral coordination around the Co(II)-center is achieved by 4-fold coordination of the six-membered chelate rings and the apical attachment of two DMAP molecules. The observed coordination figure is similar to the compound $Co(hfpip\text{-}X)_2(NOpy)_2$ (X = H,F; hfpip = 1,1,1,5,5,5-hexafluoro-4-(phenylimino)-2-pentanonate, NOpy = *N*,*N*-dipyridilaminoxyl), also based on N,O ligands.[45] In the case of Co(III) compound $Co^{III}(PyCHCOCF_3)_3$, the reaction was carried out with $PyCHCOHCF_3$ in ethanol, however, without the donor ligand DMAP. Apparently, the oxidation of Co(II) to Co(III) is accompanied by the formation of molecular hydrogen observed (as microbubbles) in the course of the reaction.

X-ray Diffraction Analysis of $Co^{II}(PyCHCOCF_3)_2(DMAP)_2$ (1). Crystals suitable for a single X-ray diffraction study were grown from a concentrated mixture of dichlormethane/ethanol (1.5/1) at room temperature. The molecular structure of $Co^{II}(PyCHCOCF_3)_2(DMAP)_2$ (**1**) is shown in Figure 3 a, while selected crystallographic data are summarized in Table 1. The compound crystallized in the triclinic space group $P\bar{1}$ with one molecule per unit cell. The central metal atom displayed an octahedral arrangement of two bidentale ligands and two DMAP molecules with the nitrogen atoms of the pyridine ring situated mutually in the *trans* position. The metal−ligand interactions of this complex are comparable with other cobalt compounds with corresponding chelating N,O ligands. In complex **1** the Co−N_{DMAP} and Co−N_{Ligand} bond lengths showed comparable values of 2.167(3) Å for Co−N_{DMAP} and 2.168(3) Å for Co−N_{Ligand}. The Co−N bond distances and Co−O bond distances (Co−O = 2.021(2) Å) are similar to the interatomic distances observed in comparable cobalt(II) complexes such as $Co(hfpip\text{-}X)_2(NOpy)_2$ (X = H,F; hfpip = 1,1,1,5,5,5-hexafluoro-4-(phenylimino)-2-pentanonate, NOpy = *N*,*N*-dipyridilaminoxyl) (Co−O = 2.008 Å av, Co−N = 2.204 Å av, Co−N_{NOpy} = 2.182 Å av)[45] and CoL_2Py_2 (Py = pyridine, L = 4-(3′,3′,3′-trifluoro-2′-oxypropylene)-2,2,5,5-tetramethyl-3-imidazoline-l-oxyl) (Co−O = 2.031(2) Å, Co−N = 2.170(2) Å, Co−N_{Py} = 2.213(2) Å).[46] The O1−Co1−Co1′, N1−Co1−N1′, and N2−Co1−N2′ bond angles of **1** display the ideal value of 180°. All other O−Co−N and N−Co−N bond angles were almost orthogonal ≈90°.

Table 1. Selected Crystallographic Data for Compounds $Co^{II}(PyCHCOCF_3)_2(DMAP)_2$ (1) and $Co^{III}(PyCHCOCF_3)_3$ (2)

	$Co^{II}(PyCHCOCF_3)_2(DMAP)_2$	$Co^{III}(PyCHCOCF_3)_3$
chemical formula	$C_{30}H_{30}F_6N_6O_2Co$	$C_{24}H_{15}F_9N_3O_3Co$
MW (g/mol)	679.53	623.32
cryst syst	triclinic	monoclinic
space group	$P\bar{1}$ (No. 2)	$P2_1/c$
a (Å)	8.796(3)	8.771(3)
b (Å)	9.262(3)	13.900(9)
c (Å)	10.669(4)	21.119(4)
α (deg)	74.34(2)	90.00
β (deg)	69.36(2)	105.11(5)
γ (deg)	83.75(2)	90.00
V, $Å^3$	783.11(49)	2485.93(64)
Z	1	4
R1 [$I_0 > 2\sigma(I)$] all data	0.0449, 0.1125	0.0474, 0.0786
wR2 [$I_0 > 2\sigma(I)$]	0.0872, 0.1012	0.1201, 0.1320
GOF	0.739	0.940

Table 2. Selected Bond Lengths (Å) and Angles (deg) in $Co^{II}(PyCHCOCF_3)_2(DMAP)_2$ (1)

Co1−O1	2.021(2)	O1−Co1−N1	89.57(10)
Co1−N1	2.168(3)	O1−Co1−N2	89.89(11)
Co1−N2	2.167(3)	O1′−Co1-N1	89.57(10)
O1−C2	1.285(4)	O1′−Co1-N2	89.89(11)
N1−C4	1.366(4)	O1−Co1−N1′	90.43(10)
N1−C8	1.350(4)	O1−Co1−N2′	90.11(11)
N2−C9	1.338(5)	N1−Co1−N2	90.95(11)
N2−C13	1.334((4)	N1−Co1−N2′	89.05(11)
N3−C11	1.356(5)	N1−Co1−N1′	180.00
N3−C14	1.440(5)	N2−Co1−N2′	180.00
N3−C15	1.461(5)	O1−Co1−O1′	180.00

Table 3. Selected Bond Lengths (Å) and Angles (deg) in $Co^{III}(PyCHCOCF_3)_3$ (2)

Co1−O1	1.888(2)	O1−Co1−N1	94.49(10)
Co1−O2	1.8859(19)	O1−Co1−N2	173.51(9)
Co1−O3	1.896(2)	O1−Co1−N3	86.28(9)
Co1−N1	1.969(2)	O1−Co1−O2	85.30(9)
Co1−N2	1.963(2)	O1−Co1−O3	88.25(9)
Co1−N3	1.953(2)	O2−Co1−O3	171.59(9)
O1−C2	1.289(4)	N1−Co1−N2	91.90(10)
N1−C4	1.350(4)	N1−Co1−N3	178.95(10)
N1−C8	1.356(4)	N2−Co1−N3	87.31(10)

X-ray Diffraction Analysis of $Co^{III}(PyCHCOCF_3)_3$ (2). Crystals from $Co^{III}(PyCHCOCF_3)_3$ were grown from a concentrated ethanol solution at room temperature. The product crystallized in the monoclinic space group $P2_1/c$ with the cobalt atom in distorted octahedral coordination due to the steric hindrance of three ligands, which are coordinated to the metal center (Figure 3 b). The octahedral complex **2** showed lower metal−oxygen and metal−nitrogen values compared to the cobalt compound $Co^{II}(PyCHCOCF_3)_2(DMAP)_2$ (**1**) (Tables 2 and 3). The significant differences in average Co−O and Co−N distances in **1** and **2** suggest different chemical oxidation states. For instance, the presence of Co(II) (Co−O = 2.021(2) Å, Co−N = 2.167(3) Å) in **1** results in longer bond lengths, when compared to **2** (Co−O = 1.890 Å av, Co−N = 1.962 Å av) and other Co(III) complexes, which are summarized in Table S 1 (Supporting Information). In addition, the bond lengths of **2** are similar to the corresponding bond of other Co(III) complexes reported in the literature such as $Co(ehmpb)_3$ (Hehmpb = *N*-ethyl-2-(29-hydroxy-39-methylphenyl)-benzimidazole) (Co−O = 1.891 Å av, Co−N = 1.932 Å av),[47] $Co^{PZ}L_3$ (^{PZ}LH = 2,4-di-*tert*-butyl-6-(5-methyl-1*H*-pyrazol-3-yl)phenol) (Co−O = 1.896 Å av, Co−N = 1.892 Å av),[48] and $Co(PhOPy)_3$(PhOHpy) = 2-(*O*-hydroxyphenyl)-pyridine) (Co−O=1.847 Å av, Co−N = 1.951 Å av).[49] The molecular structure displayed differences in the angles due to the distortion in the octahedral coordination environment. For example, the O1−Co1−N2, O2−Co1−O3, and N1−Co1−N3 angles of 173.51°, 171.59°, and 178.95° showed deviations from the ideal value (180°). In general, the Co−O and Co−N bond lengths and O1−Co1−N2, O2−Co1−O3, and N1−Co1−N3 angles are in good agreement with those found for comparable cobalt(III) complexes as mentioned above.[47−49]

Nuclear Magnetic Resonance (NMR). The precursor $Co^{II}(PyCHCOCF_3)_2(DMAP)_2$ (**1**) could not be analyzed by NMR spectroscopy due to paramagnetic properties of Co(II) compounds. In contrast to **1**, the diamagnetic complex $Co^{III}(PyCHCOCF_3)_3$ (**2**) could be completely characterized by NMR analysis, including the ^{59}Co NMR spectrum of **2**, which showed one signal at +11 095 ppm with a linewidth of 360 Hz.[50] The assignment of the three ligands $PyCHCOCF_3$, which coordinate the metal center in compound **2**, was achieved using a combination of 1D and 2D NMR experiments (^{1}H,^{1}H-COSY, ^{1}H,^{13}C-HSQC, ^{1}H,^{13}C-HMBC, ^{19}F,^{13}C-HSQC, ^{19}F,^{13}C-HMBC, ^{1}H,^{1}H-NOESY, ^{1}H,^{19}F-HOESY, ^{1}H,^{15}N-HMQC), as shown in Supporting Information Figures S 2−5. The ^{1}H and ^{19}F NMR spectra of **2** in acetone-d_6 confirmed the existence exclusively of the *mer*-isomer.[36] ^{1}H NMR spectrum showed 3 singlets centered at 5.89, 6.07, 6.27 ppm, which were assigned to the protons of the vinyl functional group. The other signals in the range 6.50−8.50 ppm could be completely assigned to every proton of the aromatic systems in **2** by means of 2D NMR spectra. All the nuclei (H, C, N, F) were unambiguously assigned to each ligand molecule in $\text{Co}^{\text{III}}(\text{PyCHCOCF}_3)_3$ (**2**). In addition, the three signals of equal intensity observed at −72.80, −72.83, −73.10 ppm in the ^{19}F NMR and the signals at 180, 188, 195 ppm, which were present in the 2D ^{1}H,^{15}N-HMQC spectrum confirmed the existence of the *mer*-isomer (**2**).

Electron Impact Mass Spectrometry (EI-MS). The mass spectral data confirmed the observations of NMR and X-ray diffraction analysis through the existence of both compounds (Supporting Information Figure S 6). $\text{Co}^{\text{II}}(\text{PyCHCOCF}_3)_2(\text{DMAP})_2$ (**1**) was characterized by the ion at *m*/*z* 435 with the highest intensity corresponding to $[\text{Co}(\text{PyCHCOCF}_3)_2]^+$ at 130 °C in the EI-MS spectrum (Figure 4). No molecular peak could be obtained due to the elimination of weakly coordinated DMAP molecules. The DMAP radical ions could be detected as a separate fragment at (*m*/*z* 122) with high intensity at the beginning of the heating process. Furthermore, the fragmentation pattern showed the loss of the ligand and fluoroalkyl group from **1** with lower intensities. EI-MS spectrum of $\text{Co}^{\text{III}}(\text{PyCHCOCF}_3)_3$ (**2**) at 135 °C exhibited the molecular peak at *m*/*z* 623 and the base peak at *m*/*z* 435 corresponding to $[\text{Co}(\text{PyCHCOCF}_3)_2]^+$. Additionally, the fragmentation pattern of the ligand PyCHCOCF_3 (*m*/*z* 189) revealed the loss of the $[\text{OCCF}_3]$ fragment and formation of $[2\text{-PyCH}_2]^+$ (*m*/*z* 92).

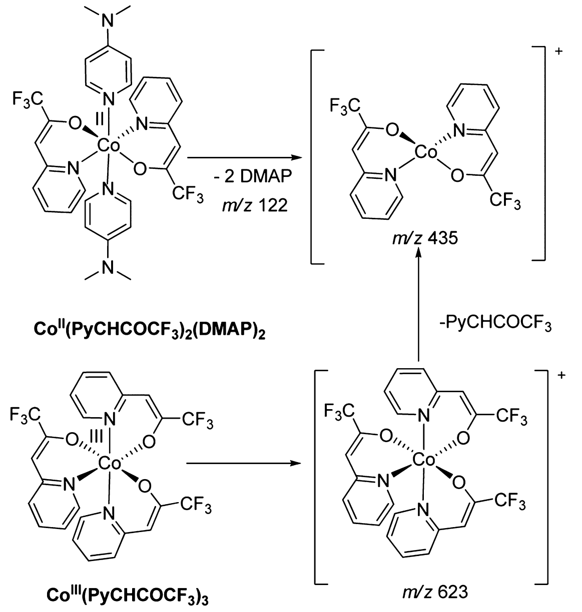

Figure 4. Fragmentation pattern of $\text{Co}^{\text{II}}(\text{PyCHCOCF}_3)_2(\text{DMAP})_2$ (**1**) and $\text{Co}^{\text{III}}(\text{PyCHCOCF}_3)_3$ (**2**).

Infrared Spectroscopy (IR). The IR spectrum of the free ligand exhibited a strong band at 1637 cm^{-1} attributed to ν(C═O) stretches. The IR spectra of $\text{Co}^{\text{II}}(\text{PyCHCOCF}_3)_2(\text{DMAP})_2$ (**1**) and $\text{Co}^{\text{III}}(\text{PyCHCOCF}_3)_3$ (**2**) displayed the C═O stretching vibrations to lower frequencies (centered around 1020 cm^{-1}; Supporting Information Figure S 7) confirming the deprotonated state and concomitant decrease in the C═O bond order due to the coordination to the metal center cobalt.[51] In addition, the bands observed within the range 1556−1535 cm^{-1} were assigned to ν(C═C) absorptions characteristic for the aromatic systems.[18] The IR spectra also revealed prominent bands in the range 1104−1172 cm^{-1} due to the C−F stretching vibrations of the ligand system PyCHCOCF_3.[45] The out-of-plane CH vibrations were observed (Supporting Information Figure S 7) at 808 cm^{-1}.[43] Co−O vibrations for **1** and **2** could be assigned at 620 and 635 cm^{-1}, whereas the Co−N bands were obtained at 578 cm^{-1} for **1** and at 580 cm^{-1} for **2**.[45]

Ultraviolet−Visible Spectroscopy (UV−Vis). The UV−vis spectrum of the representative cobalt complex **1** showed two absorptions at 264 and 279 nm attributable to π−π* transitions (Supporting Information Figure S 8). The band with a maximum at 361 nm appearing in the UV−vis spectrum is attributable to ligand−metal charge transfer. The absorptions between 612 and 696 nm could be assigned to d−d transitions. The UV−vis spectrum of complex **2** displayed two bands at 261 nm as an intense band and a broad shoulder at 292 nm, which are related to π−π* transitions. The absorption band at 365 nm and the broad band at 606 nm are attributable to ligand−metal charge transfer and d−d transition in **2**.[36]

TG and DSC Behavior of $\text{Co}^{\text{II}}(\text{PyCHCOCF}_3)_2(\text{DMAP})_2$ (1) and $\text{Co}^{\text{III}}(\text{PyCHCOCF}_3)_3$ (2). The TG and DSC analyses of $\text{Co}^{\text{II}}(\text{PyCHCOCF}_3)_2(\text{DMAP})_2$ and $\text{Co}^{\text{III}}(\text{PyCHCOCF}_3)_3$ were carried out under ambient conditions (Figure 5). The TG curves of complexes **1** and **2** showed rapid mass losses between 200 and 350 °C, indicating single-step decompositions to the oxide materials. The mass losses of 92% for **1** and 89% for **2** compare fairly well with the theoretical mass losses for the formation of Co_3O_4, 88% for **1** and 87% for **2**. The DSC analyses illustrated two exothermic events between 300 and 500 °C showing the transformation of cobalt complexes to Co_3O_4

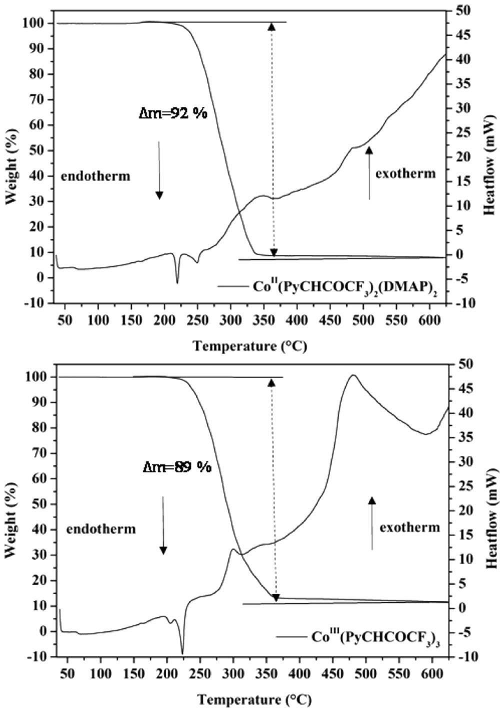

Figure 5. TG and DSC profiles of (a) $\text{Co}^{\text{II}}(\text{PyCHCOCF}_3)_2(\text{DMAP})_2$ (**1**) and (b) $\text{Co}^{\text{III}}(\text{PyCHCOCF}_3)_3$ (**2**).

upon thermal treatment at 300 °C. The XRD analyses of both obtained residues at 800 °C proved the formation of crystalline Co_3O_4 (Supporting Information Figure S 9). In addition, both compounds showed two endothermic peaks in the range 200−250 °C associated with their sublimation, which was suggestive of the good volatility of the complexes, and melting of $Co^{II}(PyCHCOCF_3)_2(DMAP)_2$ (T_S = 219 °C, T_M = 250 °C) and $Co^{III}(PyCHCOCF_3)_3$ (T_S = 204 °C, T_M = 225 °C).

Chemical Vapor Deposition Process: One-Dimensional Growth and Characterization of Co_3O_4. The precursors $Co^{II}(PyCHCOCF_3)_2(DMAP)_2$ (**1**) and $Co^{III}(PyCHCOCF_3)_3$ (**2**) were used in a low-pressure CVD process to grow cobalt oxide nanostructures. Deposition of both compounds at 800 °C for 90 min on Si and Al_2O_3 substrates produced crystalline Co_3O_4, as confirmed by X-ray diffraction analyses of as-grown films. The main signals in XRD pattern were indexed to the Co_3O_4 phase as shown in Figure 6.

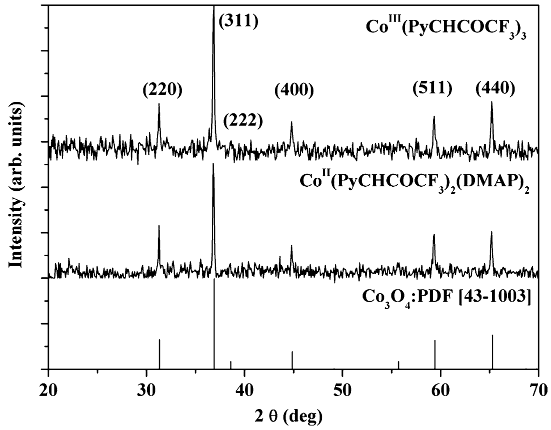

Figure 6. X-ray diffraction pattern (XRD) of as grown Co_3O_4 nanowires (Si) in CVD of **1** and **2**.

Nevertheless, the cobalt(III) oxide, Co_2O_3, could not be obtained using the precursor $Co^{III}(PyCHCOCF_3)_3$, possibly due to the high substrate temperature (800 °C) that makes the stabilization of a thermodynamically labile phase Co_2O_3 unfavorable. Various attempts to obtain Co_2O_3 by changing the deposition temperatures were not successful presumably due to thermodynamic impediments. It is likely that this phase may exist at lower deposition temperatures, which would however require an alternative precursor activation mechanism such as application of cold plasmas. X-ray photoelectron spectroscopy (XPS) on the obtained Co_3O_4 (Figure 7) showed the nanowires of **1** and **2**, to predominantly contain Co (Co $2p_{1/2}$ = 794 eV, Co $2p_{3/2}$ = 779 eV), O (O 1s = 529 eV), and C (C 1s = 284 eV) elements, whereas the presence of carbon is caused by the organic residues formed in the decomposition of the ligand $PyCHCOCF_3$.[53,54] No fluorine contamination could be observed on the surface of Co_3O_4 nanowires. Furthermore, the Raman studies of the synthesized nanostructures verified the presence of Co_3O_4 crystalline phase.

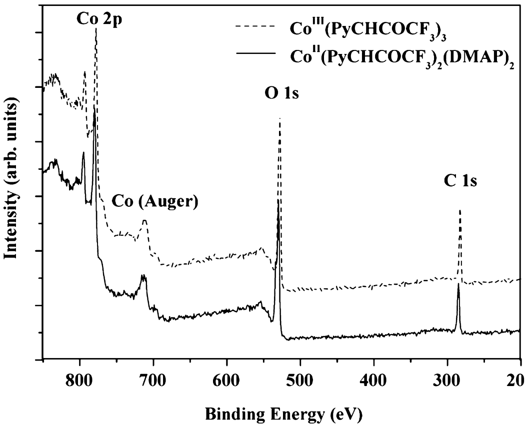

Figure 7. X-ray photoelectron spectrum of Co_3O_4 deposits (Si) obtained in the CVD of **1** and **2**.

The Raman spectra of Co_3O_4 deposits obtained in the CVD of **1** and **2** exhibited four expected Raman active modes (A_{1g}, F_{2g1}, F_{2g2}, and E_g) corresponding to the cobalt oxide spinel structure, which were found to be in good agreement with other Raman spectral data reported for cobalt oxides.[55,56] Figure 8 depicts the Raman peaks correspond to the E_g (482 cm^{-1}), F_{2g} (195 and 620 cm^{-1}), and A_{1g} (690 cm^{-1}) modes of the Co_3O_4 phase.

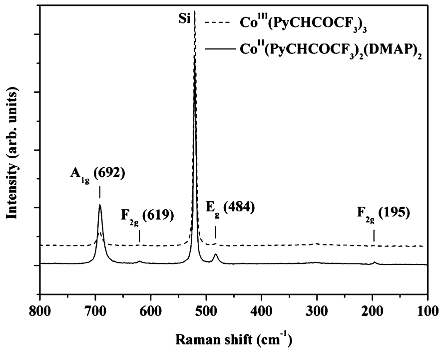

Figure 8. Raman spectra of Co_3O_4 films (Si) obtained in the CVD of **1** and **2**.

The representative SEM images (Figure 9) displayed that Co_3O_4 nanowires obtained from **1** and **2** exhibited significantly different morphologies despite similar phase composition indicating that the different valence states of cobalt (Co^{II} and Co^{III}) in precursor molecules evidently influenced their decomposition patterns in the CVD process as also indicated by their significantly different decomposition temperatures. The growth conditions chosen in this work ($T_{substrate}$ = 800−900 °C, $T_{precursor}$ = 140−150 °C) were different from those reported for the metal-catalyzed growth of metal oxide nanowires.[20] In contrast to the previous reports, Co_3O_4 nanowires were grown for the first time without employing any metal catalysts or growth templates.

During the deposition process, oxygen was introduced in the system to facilitate the growth of the Co_3O_4 nanowires as the Co:O ratio in the precursor is insufficient to produce Co_3O_4 since as-obtained CVD deposits without any external oxygen source were found to be amorphous. The precursor and oxygen fluxes were regulated following the feedback of the pressure monitor coupled to the CVD reactor. Anisotropic Co_3O_4 nanowires on Si(100) and polycrystalline Al_2O_3 were obtained using the precursor $Co^{II}(PyCHCOCF_3)_2(DMAP)_2$ after a deposition time of 90 min (Figure 9a,b). Typical diameters of the nanowires were found to be around 50 nm, with lengths lying in the range of tens of micrometers (Figure 10a,b). In comparison to as-grown Co_3O_4 nanowires in CVD of **1**, the

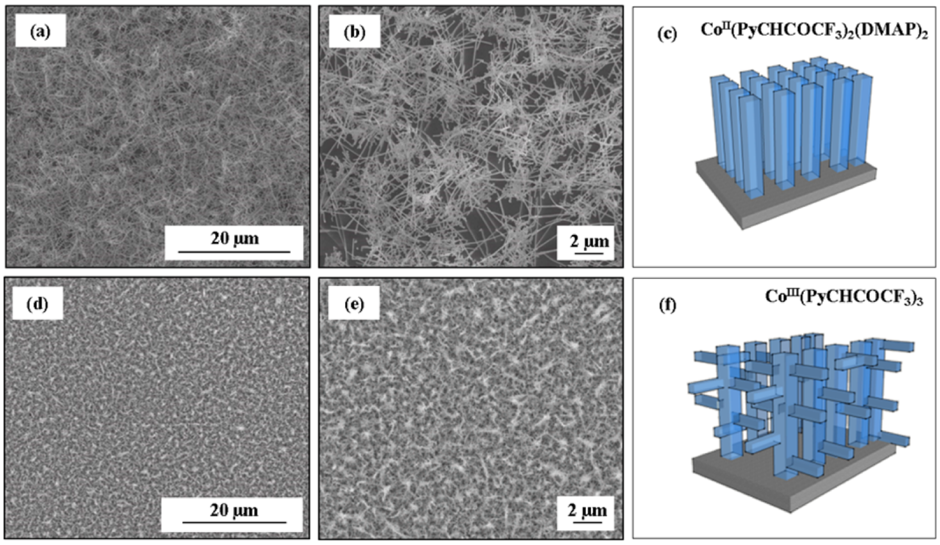

Figure 9. Scanning electron micrographs of the deposited Co_3O_4 nanowires obtained from (a, b) $Co^{II}(PyCHCOCF_3)_2(DMAP)_2$ (**1**) and (d, e) $Co^{III}(PyCHCOCF_3)_3$ (**2**). Schemes c and f present the 1D growth of unbranched and branched nanowires of **1** and **2**.

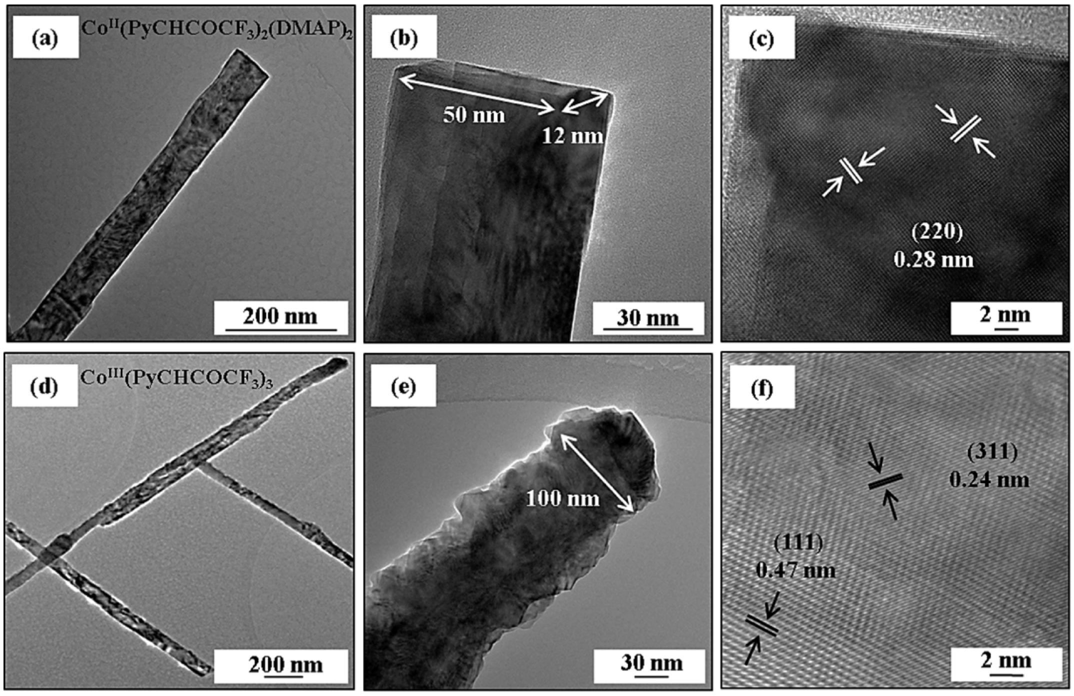

Figure 10. High-resolution transmission electron microscopy (HR-TEM) images of Co_3O_4 nanowires (Si) obtained from **1** (a–c) and **2** (d–f).

SEM and TEM micrographs of as-grown nanowires on Si(100) and Al_2O_3 obtained from $Co^{III}(PyCHCOCF_3)_3$ (**2**) showed a branched structure with an average diameter of 100 nm (Figure 9d,e and Figure 10d,e). The corresponding schematic illustration of nanowire morphologies is depicted in Figure 9 c,f, which reveals the unique difference in the decomposition and growth processes manifested in individual and branched structures obtained in the case of **1** and **2**, respectively. The nanoarchitecture and structural characteristics of cobalt oxides analyzed by high-resolution transmission electron microscopy (HR-TEM) confirmed that highly crystalline Co_3O_4 nanowires were formed during the CVD process. The HR-TEM image of as grown Co_3O_4 nanowires in the CVD of **1** showed lattice fringes with an interplanar distance of 0.28 nm corresponding to the (220) plane of Co_3O_4, which is in good agreement with XRD data (Figure 10c). For Co_3O_4 nanowires obtained from **2**, the lattice fringes of 0.24 and 0.47 nm corresponded to the (311) and (111) planes of the spinel Co_3O_4, respectively (Figure 10f).

Humidity Sensing Properties of Co_3O_4 Nanowires. The potential of the CVD-grown Co_3O_4 nanowires for humidity sensing was demonstrated by monitoring the resistivity change (dc resistance) in the device structures kept under different ambient conditions of water vapor and synthetic air (Figure 11). The response of both Co_3O_4 nanowire arrays ($R(H_2O)/R(Air)) - 1 \times 100\%$) exhibited a highly linear relationship between the resistivity change with increasing humidity concentration ($R^2 \sim 0.98$), indicating the suitability of Co_3O_4 nanowires for humidity sensing (Figure 12). Screening of the response at different temperatures revealed an optimal working

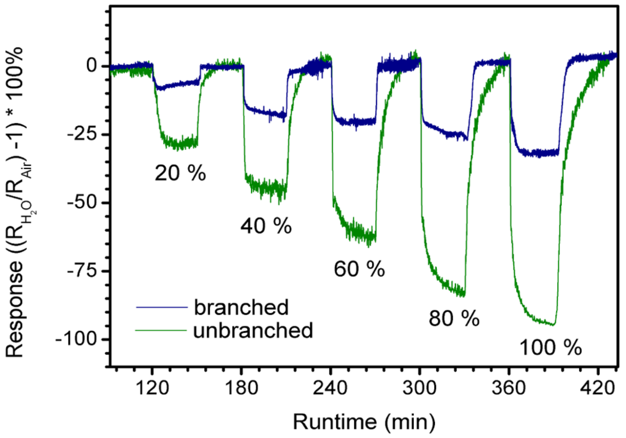

Figure 11. Humidity sensing properties of unbranched and branched Co_3O_4 nanowires of **1** and **2** on Al_2O_3 at 30 °C.

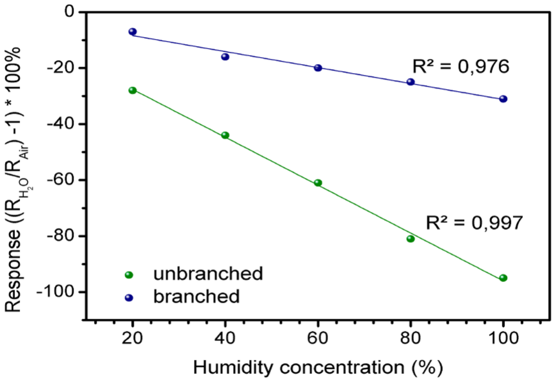

Figure 12. Sensor response of obtained unbranched and branched Co_3O_4 nanowires in the CVD of **1** and **2** vs humidity concentration.

temperature of 30 °C. At lower temperatures the resistivity of the Co_3O_4 nanowire arrays was too high to gather reproducible values (≥ 5 GΩ), whereas at higher temperatures the response intensity and linearity decreased possibly due to catalytic decomposition of water molecules. The sensitivity (defined as the slope of the response vs relative humidity plot in Figure 11) was found to be -0.86 ± 0.02 for the as-grown unbranched nanowires of **1** and -0.26 ± 0.02 for the branched counterparts obtained of **2**. The response time after each pulse (time until 95% response is achieved) was around 7 min (unbranched Co_3O_4) and 6 min (branched Co_3O_4) and the recovery time (time until 95% recovery) around 8 min (unbranched Co_3O_4) and 17 min (branched Co_3O_4), respectively.

Both values are reproducible and independent of the relative humidity. Extrapolation of the response indicated that both Co_3O_4 nanowire arrays can detect humidity at concentrations below 20%, while the unbranched nanowires are sensitive down to 1%. The superior sensitivity of unbranched nanowires might be attributed to the higher accessibility of cobalt oxide to the analyte molecules. The accompanying inferior sensing kinetics of unbranched nanowires is possibly due to the higher surface area and more efficient charge transport in the branched nanowires due to multiple material junctions. Alternatively, the facile formation of rooted hydroxyl groups and high sticking coefficient of water can also prevent a fast dehydration process manifesting a sluggish sensing kinetics. The degree of hysteresis was assumed to be negligible due to the good linearity and reproducibility of the response; however, further investigations are necessary for a detailed comparison. When compared with the results published by Yang et al. about humidity sensing using cobalt oxide nanosheets,[57] both Co_3O_4 nanowire arrays appeared to possess superior properties particularly regarding the linearity of the response, which is important for the quantification of the humidity. Humidity sensing is in general mainly driven either by a surface conduction mechanism occurring in the physisorbed water layers or by a variation of the semiconductor conductivity caused by chemical surface reactions.[57,58] As the resistance of both Co_3O_4 nanowire arrays was found to be very high, the surface conduction mechanism appears to be predominant in this case. Here the conduction is due to the Grotthuss mechanism in which protons tunnel from one physisorbed water molecule to the next via hydrogen bonding that universally exists in liquid-phase water.[59] The sensing results clearly demonstrate that the choice of precursor in material synthesis can enormously influence the functional behavior of the final solid-state phase. Nevertheless, the nanostructured surfaces in both cases allow humidity detection close to the room temperature making them promising sensor materials.

■ CONCLUSIONS

In conclusion, facile synthesis of two cobalt complexes in different oxidation states (Co^{2+} and Co^{3+}) was successfully demonstrated by employing a redox-supportive ligand system based on an alkenol backbone substituted by both electron-donating (aromatic units) and electron-withdrawing ($-CF_3$) groups. In addition, Co_3O_4 nanowires were grown without preapplication of metal particles as catalysts which is necessary for a typical vapor−liquid−solid (VLS) type growth.[60] Investigations of experimental conditions revealed the influence of gas phase decomposition processes that delivered unbranched and branched Co_3O_4 nanowires in the CVD of **1** and **2**, respectively. The formation of pure cobaltite phase in both the cases involves the oxidation ($Co^{2+} \rightarrow Co^{3+}$) of metal center in **1** and reduction ($Co^{3+} \rightarrow Co^{2+}$) in **2** and indicates a thermodynamically controlled CVD process as the desired cobalt(III) oxide phase could not be obtained. The one-dimensional and hyperbranched morphologies of the Co_3O_4 nanowires made them efficient materials for humidity sensing close to the room temperature (30 °C). The differential sensing behavior despite similar chemical composition of the CVD deposits points out the morphology influence of the materials, showing superior sensitivity by **1** that enables rapid response and sensing kinetics when compared to hyperbranched nanowires **2**.

■ ASSOCIATED CONTENT

Ⓢ Supporting Information

NMR, EI-MS, IR, and UV−vis data of synthesized cobalt complexes. X-ray crystallographic data files in CIF format for compounds $Co^{II}(PyCHCOCF_3)_2(DMAP)_2$ and $Co^{III}(PyCHCOCF_3)_3$. This material is available free of charge via the Internet at http://pubs.acs.org.

■ AUTHOR INFORMATION

Corresponding Author

*E-mail: sanjay.mathur@uni-koeln.de.

Notes

The authors declare no competing financial interest.

■ ACKNOWLEDGMENTS

The authors would like to thank the University of Cologne and the “Fonds der Chemischen Industrie” (FCI) for financial support. Additionally, we are thankful to Dr. Trilok Singh for Raman and Mr. Johannes Schläfer for HR-TEM measurements.

■ REFERENCES

(1) Chen, M.; Hallstedt, B.; Gauckler, L. J. *J. Phase Equilib.* **2003**, *24*, 212−227.

(2) Chenavas, J.; Joubert, J. C. *Solid State Commun.* **1971**, *9*, 1057−1060.

(3) Ma, C. Y.; Mu, Z.; Li, J. J.; Jin, Y. G.; Cheng, J.; Lu, G. Q.; Hao, Z. P.; Qiao, S. Z. *J. Am. Chem. Soc.* **2010**, *132*, 2608−2613.

(4) Hu, L.; Peng, Q.; Li, Y. *J. Am. Chem. Soc.* **2008**, *130*, 16136−16137.

(5) Zheng, M.; Cao, J.; Liao, S.; Liu, J.; Chen, H.; Zhao, Y.; Dai, W.; Ji, G.; Cao, J.; Tao, J. *J. Phys. Chem. C* **2009**, *113*, 3887−3894.

(6) Wang, H.; Zhang, L.; Tan, X.; Holt, C. M. B.; Zahiri, B.; Olsen, B. C.; Mitlin, D. *J. Phys. Chem. C* **2011**, *115*, 17599−17605.

(7) Yang, X.; Fan, K.; Zhu, Y.; Shen, J.; Jiang, X.; Zhao, P.; Luan, S.; Li, C. *ACS Appl. Mater. Interfaces* **2013**, *5*, 997−1002.

(8) Guo, B.; Li, C.; Yuan, Z. *J. Phys. Chem. C* **2010**, *114*, 12805−12817.

(9) Li, C. C.; Yin, X. M.; Wang, T. H.; Zeng, H. C. *Chem. Mater.* **2009**, *21*, 4984−4992.

(10) Jiao, Q.; Fu, M.; You, C.; Zhao, Y.; Li, H. *Inorg. Chem.* **2012**, *51*, 11513−20.

(11) Xi, L.; Tran, P. D.; Chiam, S. Y.; Bassi, P. S.; Mak, W. F.; Mulmudi, H. K.; Batabyal, S. K.; Barber, J.; Say, J.; Loo, C.; Wong, L. H. *J. Phys. Chem. C* **2012**, *116*, 3−8.

(12) Sun, C.; Su, X.; Xiao, F.; Niu, C.; Wang, J. *Sens. Actuators, B* **2011**, *157*, 681−685.

(13) Man, L.; Niu, B.; Xu, H.; Cao, B.; Wang, J. *Mater. Res. Bull.* **2011**, *46*, 1097−1101.

(14) He, T.; Chen, D.; Jiao, X.; Xu, Y. *Langmuir* **2004**, *20*, 8404−8408.

(15) Nethravathi, C.; Sen, S.; Ravishankar, N.; Rajamathi, M.; Pietzonka, C.; Harbrecht, B. *J. Phys. Chem. B* **2005**, *109*, 11468−11472.

(16) Barakat, N. A. M.; Khil, M. S.; Sheikh, F. A.; Kim, H. Y. *J. Phys. Chem. C* **2008**, *112*, 12225−12233.

(17) Ding, Y.; Wang, Y.; Su, L.; Bellagamba, M.; Zhang, H.; Lei, Y. *Biosens. Bioelectron.* **2010**, *26*, 542−548.

(18) Bandoli, G.; Barreca, D.; Gasparotto, A.; Maccato, C.; Seraglia, R.; Tondello, E.; Devi, A.; Fischer, R. A.; Winter, M. *Inorg. Chem.* **2009**, *48*, 82−89.

(19) Barreca, D.; Comini, E.; Gasparotto, A.; Maccato, C.; Pozza, A.; Sada, C.; Sberveglieri, G.; Tondello, E. *J. Nanosci. Nanotechnol.* **2010**, *10*, 8054−8061.

(20) Maruyama, T.; Nakai, T. *Sol. Energy Mater.* **1991**, *23* (1), 25.

(21) Barreca, D.; Devi, A.; Fischer, R. A.; Bekermann, D.; Gasparotto, A.; Gavagnin, M.; Maccato, C.; Tondello, E.; Bontempi, E.; Depero, L. E.; Sada, C. *CrystEngComm* **2011**, *13*, 3670−3673.

(22) Barreca, D.; Fornasiero, P.; Gasparotto, A.; Gombac, V.; Maccato, C.; Pozza, A.; Tondello, E. *Chem. Vap. Deposition* **2010**, *16*, 296−300.

(23) Burriel, M.; Garcia, G.; Santiso, J.; Abrutis, A.; Saltyte, Z.; Figueras, A. *Chem. Vap. Deposition* **2005**, *11*, 106−111.

(24) Fiz, R.; Hernandez-Ramirez, F.; Fischer, T.; Lopez-Conesa, L.; Estrade, S.; Peiro, F.; Mathur, S. *J. Phys. Chem. C* **2013**, *117*, 10086−10094.

(25) Pan, J.; Shen, H.; Xiao, L.; Born, P.; Mader, W. *J. Phys. Chem. C* **2011**, *115*, 17265−17269.

(26) Zamani, R.; Fiz, R.; Pan, J.; Fischer, T.; Mathur, S.; Morante, J. R.; Arbiol, J. *CrystEngComm* **2013**, *15*, 4532−4539.

(27) Barth, S.; Estrade, S.; Hernandez-Ramirez, F.; Peiro, F.; Arbiol, J.; Romano-Rodriguez, A.; Morante, J. R.; Mathur, S. *Cryst. Growth Des.* **2009**, *9*, 1077−1081.

(28) Veith, M.; Mathur, S.; Mathur, C. *Polyhedron* **1998**, *17*, 1005−1034.

(29) Tyczkowski, J.; Kapica, R.; Łojewska, J. *Thin Solid Films* **2007**, *515*, 6590−6595.

(30) Lane, B. P. A.; Oliver, P. E.; Wright, P. J.; Reeves, C. L.; Pitt, A. D. 1998, 183−186.

(31) Dormans, G. J. M.; Meekes, G. J. B. M.; Staring, E. G. J. *J. Cryst. Growth* **1991**, *114*, 364−372.

(32) Giebelhaus, I.; Varechkina, E.; Fischer, T.; Rumyantseva, M.; Ivanov, V.; Gaskov, A.; Morante, J. R.; Arbiol, J.; Tyrra, W.; Mathur, S. *J. Mater. Chem. A* **2013**, *1*, 11261−11268.

(33) Giebelhaus, I.; Müller, R.; Tyrra, W.; Pantenburg, I.; Fischer, T.; Mathur, S. *Inorg. Chim. Acta* **2011**, *372*, 340−346.

(34) Appel, L.; Fiz, R.; Tyrra, W.; Mathur, S. *Dalton Trans.* **2012**, *41*, 1981−1990.

(35) Brückmann, L.; Tyrra, W.; Stucky, S.; Mathur, S. *Inorg. Chem.* **2012**, *51*, 536−542.

(36) Root, B. Y. C. A.; Rowe, J. A. Y. E.; Veening, H. *Inorg. Chem.* **1971**, *10*, 1195−1197.

(37) Gulino, A.; Fiorito, G.; Fragalà, I. *J. Mater. Chem.* **2003**, *13*, 861−865.

(38) Barreca, D.; Massignan, C.; Inorganica, C.; Analitica, M.; Loredan, V.; Padova, I.-; Daolio, S.; Fabrizio, M.; Piccirillo, C.; Armelao, L.; Tondello, E. *Chem. Mater.* **2001**, *13*, 588−593.

(39) *X-Area 1.16*; Stoe and Cie GmbH: Darmstadt, Germany, 2003.

(40) Farrugia, L. J. *J. Appl. Crystallogr.* **1999**, *32*, 837−838.

(41) Altomare, A.; Cascarano, G.; Giacovazzo, C.; Guagliardi, A. *J. Appl. Crystallogr.* **1993**, *26*, 343−350.

(42) Sheldrick, G. M. *SHELXL-97, Programs for Crystal Structure Analysis*; University of Göttingen: Göttingen, Germany, 1997.

(43) Lehnen, T.; Valldor, M.; Nižňanský, D.; Mathur, S. *J. Mater. Chem. A* **2014**, *2*, 1862−1868.

(44) Lehnen, T.; Zopes, D.; Mathur, S. *J. Mater. Chem.* **2012**, *22*, 17732−17736.

(45) Murashima, K.; Watanabe, T.; Kanegawa, S.; Yoshihara, D.; Inagaki, Y.; Karasawa, S.; Koga, N. *Inorg. Chem.* **2012**, *51*, 4982−4993.

(46) Romanenko, G. V.; Fursova, E. Yu.; Ovcharenko, V. I. *J. Struct. Chem.* **1999**, *40*, 580−588.

(47) Crane, J. D.; Sinn, E.; Tann, B. *Polyhedron* **1999**, *18*, 1527−1532.

(48) Zats, G. M.; Arora, H.; Lavi, R.; Yufit, D.; Benisvy, L. *Dalton Trans.* **2011**, *40*, 10889−10896.

(49) Ganis, P.; Saporito, A.; Vitagliano, A. *Inorg. Chim. Acta* **1988**, *142*, 75−79.

(50) Yamasaki, A. *J. Coord. Chem.* **1991**, *24*, 211−260.

(51) Gulino, A.; Dapporto, P.; Rossi, P.; Anastasi, G.; Fragalà, I. *J. Mater. Chem.* **2004**, *14*, 2549−2553.

(52) Morris, M. L.; Moshier, R. W.; Sievers, R. E. *Inorg. Chem.* **1963**, *2*, 411−412.

(53) Liang, Y.; Li, Y.; Wang, H.; Zhou, J.; Wang, J.; Regier, T.; Dai, H. *Nat. Mater.* **2011**, *10*, 780−6.

(54) Baek, J. H.; Park, J. Y.; Hwang, A. R.; Kang, Y. C. *Bull. Korean Chem. Soc.* **2012**, *33*, 1242−1246.

(55) Yang, J.; Liu, H.; Martens, W. N.; Frost, R. L. *J. Phys. Chem. C* **2010**, *114*, 111−119.

(56) Tang, C.-W.; Wang, C.-B.; Chien, S.-H. *Thermochim. Acta* **2008**, *473*, 68−73.

(57) Yang, M.-Z.; Dai, C.-L.; Shih, P.-J.; Chen, Y.-C. *Microelectron. Eng.* **2011**, *88*, 1742−1744.

(58) Traversa, E. *Sens. Actuators, B* **1995**, *23*, 135−156.

(59) Chen, Z.; Lu, C. *Sens. Lett.* **2005**, *3*, 274−295.

(60) Wu, Y.; Yang, P. *Chem. Mater.* **2000**, *12*, 605−607.